PHYSICS

Observation of robust zero-energy state and enhanced superconducting gap in a trilayer heterostructure of $MnTe/Bi_2Te_3/Fe(Te, Se)$

Shuyue Ding[1]†, Chen Chen[1]†, Zhipeng Cao[2]†, Di Wang[2]†, Yongqiang Pan[3], Ran Tao[1], Dongming Zhao[1], Yining Hu[1], Tianxing Jiang[1], Yajun Yan[4], Zhixiang Shi[3], Xiangang Wan[2,5], Donglai Feng[4,5,6,7], Tong Zhang[1,5,6]*

Copyright © 2022 The Authors, some rights reserved; exclusive licensee American Association for the Advancement of Science. No claim to original U.S. Government Works. Distributed under a Creative Commons Attribution NonCommercial License 4.0 (CC BY-NC).

The interface between magnetic material and superconductors has long been predicted to host unconventional superconductivity, such as spin-triplet pairing and topological nontrivial pairing state, particularly when spin-orbital coupling (SOC) is incorporated. To identify these unconventional pairing states, fabricating homogenous heterostructures that contain such various properties are preferred but often challenging. Here, we synthesized a trilayer-type van der Waals heterostructure of $MnTe/Bi_2Te_3/Fe(Te, Se)$, which combined s-wave superconductivity, thickness-dependent magnetism, and strong SOC. Via low-temperature scanning tunneling microscopy, we observed robust zero-energy states with notably nontrivial properties and an enhanced superconducting gap size on single unit cell (UC) MnTe surface. In contrast, no zero-energy state was observed on 2-UC MnTe. First-principle calculations further suggest that the 1-UC MnTe has large interfacial Dzyaloshinskii-Moriya interaction and a frustrated AFM state, which could promote noncolinear spin textures. It thus provides a promising platform for exploring topological nontrivial superconductivity.

INTRODUCTION

When materials with different quantum orders meet at the interface, new physical phenomena may emerge and bring potential applications. A well-known example is the ferromagnet (s-wave)–superconductor interface. Intensive studies have shown that while the spin-singlet pairing potential decays fast in ferromagnet, an odd-frequency spin-triplet pairing state can be induced (*1*, *2*). A spin rotation layer or spin-orbital coupling (SOC) can further stabilize triplet Cooper pair and generate spin-polarized supercurrent (*3*–*6*), which is of particular interest in spintronic applications. Recently, there is increased research on magnet-superconductor interface with strong SOC or noncolinear spin textures, as these systems may give rise to topological superconductivity (TSC) (*7*–*19*). The chiral magnetic atom chain grown on strong SOC superconductors was considered as its one-dimensional (1D) case (*7*, *8*), which is in analogy to the semiconductor nanowire–superconductor hybrids under Zeeman field (*20*, *21*). In the 2D case, magnetic moments arranged on superconductor can form Shiba lattice (*9*, *10*). Various types of chiral spin textures are predicted to induce effective p-wave pairing, and Majorana boundary mode will emerge when the system enters topological phase. The merits of these potential TSC platforms are that they do not require external field, and the spin textures could be controlled electronically (*22*, *23*). Besides, theoretical works also predicted that if a 3D topological insulator (TI) layer is inserted in between ferromagnet and superconductor layers, 2D TSC/chiral Majorana edge mode can be induced because of different gap opening in the top/bottom surface states (*24*, *25*).

To experimentally identify these unconventional pairing states, fabrication of high-quality magnet-superconductor heterostructures with proper interface is highly desired since unconventional pairing is often sensitive to disorder or inhomogeneity, and local probe study such as scanning tunneling microscopy (STM) favors atomically flat surface/interface. Several recent STM studies (*26*–*29*) have demonstrated the advantage of using layered magnetic material (such as transition metal chalcogenides) to make these heterostructures, as they can be grown epitaxially and persist magnetism down to single-layer limit. Moreover, it is also preferred to introduce strong SOC material or topological band structure (such as a TI) into the heterostructure, as they can further promote the TSC phase. In particular, it was shown that if combining strong SOC and inversion asymmetry (which always happens at interface) in a magnetic system, then large Dzyaloshinskii-Moriya interactions (DMI) can be induced and give rise to noncolinear spin textures (*30*–*32*). Transport studies on ferromagnet-TI interfaces have observed signatures of skyrmion-like spin structure (*33*–*35*). Therefore, it would be very promising to fabricate a magnet-superconductor heterostructure incorporated with strong SOC materials for exploring potential unconventional superconductivity. However, so far, this kind of heterostructure is rarely reported.

In this work, we successfully synthesized a trilayer-type heterostructure of $MnTe/Bi_2Te_3/Fe(Te, Se)$ that has atomically sharp interface. It combines the magnetism of MnTe, strong SOC from Bi_2Te_3 and superconductivity from Fe(Te, Se). Via low-temperature STM, we observed zero-energy conductance peaks (ZECP) on many regions of 1–unit cell (UC)–thick MnTe surface and an enlarged superconducting gap in comparison to that of Fe(Te, Se). The ZECPs show several distinguished properties: They are not correlated to the observed

[1]Department of Physics, State Key Laboratory of Surface Physics and Advanced Material Laboratory, Fudan University, Shanghai 200438, China. [2]National Laboratory of Solid State Microstructures and School of Physics, Nanjing University, Nanjing 210093, China. [3]School of Physics and Key Laboratory of MEMS of the Ministry of Education, Southeast University, Nanjing 211189, China. [4]Department of Physics, University of Science and Technology of China, Hefei 230026, China. [5]Collaborative Innovation Center of Advanced Microstructures, Nanjing 210093, China. [6]Shanghai Research Center for Quantum Sciences, Shanghai 201315, China. [7]National Synchrotron Radiation Laboratory, University of Science and Technology of China, Hefei 230026, China.
*Corresponding author. Email: tzhang18@fudan.edu.cn
†These authors contributed equally to this work.

surface defects, robust under out-of-plane field, and display saturated conductance at low tunneling barriers. Meanwhile, no in-gap state was observed on 2-UC MnTe surface. Our first-principle calculations suggest that 1-UC MnTe with the Bi_2Te_3 host large interfacial DMI and a frustrated antiferromagnetic (AFM) state, which can promote noncolinear spin textures. Thus, the emergence of ZECPs and their nontrivial features may originate from topological pairing state.

RESULTS

Growth and STM characterization of the heterostructure

MnTe is a layered AFM insulator with a NiAs-type hexagonal structure (which has an in-plane ferromagnetic order and AFM coupling between each plane) (*36*, *37*), while bulk Bi_2Te_3 is a 3D TI whose UC has a "quintuple layer" structure along *c* axis (*38*). We fabricated the MnTe/Bi_2Te_3/Fe(Te, Se) heterostructure via ultrahigh vacuum molecular beam epitaxy (UHV-MBE). Bi_2Te_3 (1 UC) was firstly grown on as-cleaved Fe(Te, Se) surface, followed by the growth of 1- to 2-UC MnTe film and post-annealing. The sample was then transferred to a low-temperature STM with calibrated resolution (fig. S1). Detailed experimental procedures are described in Materials and Methods. The 1-UC Bi_2Te_3 here not only provides strong SOC to the interface but also acts as a necessary buffer layer for MnTe growth, as its in-plane lattice constant (0.437 nm) is close to MnTe (0.419 nm) and has a Te-terminated surface. Moreover, previous studies have shown that Bi_2Te_3 has good superconducting proximity effect when grown on Fe(Te, Se) (*39*, *40*).

Figure 1A shows a large-scale STM image of as-grown MnTe/Bi_2Te_3/Fe(Te, Se) heterostructure. The surface contains various types of atomically flat terraces, including 1-UC Bi_2Te_3, 1- or 2-UC MnTe on 1-UC Bi_2Te_3, and bare Fe(Te, Se) substrate. They can be identified through the step height (reflected by different colors in Fig. 1A) and the in-plane lattice structure. Figure 1B shows a line profile taken across several terraces in Fig. 1A. The 1-UC Bi_2Te_3 has its characteristic height of ~1.0 nm, and 1-UC MnTe has a height of 0.32 nm, which corresponds to the single UC thickness in their bulk form (*37*, *38*). Panels C and D of Fig. 1 are zoomed-in images of 1-UC Bi_2Te_3 and 1-UC MnTe surfaces, while panels E and F of Fig. 1 show their atomic lattice, respectively. Both of the two surfaces have a hexagonal lattice with a constant of 0.43 nm and are oriented in the same direction, which indicates that MnTe is epitaxially grown on Bi_2Te_3 (sketched in Fig. 1B). Meanwhile, the exposed Fe(Te, Se) remains intact with a square lattice (Fig. 1G), indicative of a sharp interface. We note that this MnTe/Bi_2Te_3 epitaxial structure is different from the $MnBi_2Te_4$ film reported in (*41*), which is also grown by MBE but with different growth/annealing conditions. A similar epitaxial structure was reported in the growth of MnSe on Bi_2Se_3 surface (*42*). As seen in Fig. 1 (C and D), there are certain amounts of point defects on both Bi_2Te_3 and MnTe surfaces, which locate at the hollow site of Te lattice, as indicated in Fig. 1 (E and F). They are thus likely the substitutional defects of Bi or Mn (*43*). Nonetheless, these defects do not affect the superconductivity in either MnTe or Bi_2Te_3 surface noticeably, as shown in fig. S2 and further discussion below.

Having identified the interface structure, the electronic states are studied by tunneling spectroscopy. Figure 1H shows large energy scale (±1 eV) dI/dV spectra taken on different surfaces. On Fe(Te, Se) substrate and 1-UC Bi_2Te_3, the line shapes of the spectra are similar to previous studies (*39*, *40*). For 1-UC MnTe on Bi_2Te_3/Fe(Te, Se), the dI/dV displays a large bandgap about 500 meV wide, which is consistent with the idea that bulk MnTe is an insulator. However, the E_F of 1-UC MnTe locates close to the upper edge of the gap. This is likely due to electron doping effect induced by interfacial charge transfer. Figure 2 (A and B) shows the quasiparticle interference (QPI) measurement on 1-UC MnTe, which further revealed that a shallow electron pocket crossed E_F, with a band bottom at −60(±10) meV (see fig. S3 for additional QPI data). This indicates that the electrons in 1-UC MnTe will participate in superconductivity (QPI patterns are also observed on 1-UC Bi_2Te_3 but displays a different dispersion; see fig. S4). As for the 2-UC MnTe, there is still a flat insulating gap, but the E_F is at the gap center, indicating a weakened doping effect.

The low-energy dI/dV spectra that reflect superconducting state are then measured at $T = 0.4$ K on different surfaces, as summarized in Fig. 2C. The superconducting spectrum of Fe(Te, Se) substrate is fully gapped with multiple pairs of coherence peaks at ±1.5, ±1.9, and ±2.5 meV, respectively. We note that similar gaps were also reported in previous STM study and were assigned to different bands of Fe(Te, Se) (*44*). The gap spectrum of 1-UC Bi_2Te_3 share similarities with Fe(Te, Se): Its major coherence peaks are at ±1.9 meV, while kink features at ±1.5 and ±2.5 meV can also be observed. This indicates a good superconducting proximity effect in Bi_2Te_3. However, for 1-UC MnTe, the spectrum displays rather unconventional behavior. First, in about 50% regions, a large "U"-shaped gap with a size of 2.9 meV (defined by the lowest kink feature at gap edge) is observed, as the one shown in Fig. 2C (red curve). Figure 2D displays how the gap evolves at a boundary between 1-UC Bi_2Te_3 and 1-UC MnTe, in which one can clearly see the gap enhancement in 1-UC MnTe region. Figure 2E shows the temperature dependence of the 1-UC MnTe gap. It almost disappeared above 13.6 K, which cannot be ascribed to the thermo broadening only (by comparing with numerically broadened spectra in Fig. 2E). This indicates that the gap of MnTe is still a proximity gap induced by Fe(Te, Se) (similar temperature dependence was also observed for the gap of 1-UC Bi_2Te_3; see fig. S5). Moreover, we have also observed vortex state in the gapped region of 1-UC MnTe (fig. S6), which further confirms its superconducting nature. The enlarged gap size in 1-UC MnTe is quite unexpected as one usually observes reduced gap in magnet/superconductor interfaces. Besides the enhanced gap, in other regions of 1-UC MnTe, we observed multiple in-gap states and zero-energy modes, which will be discussed in detail below. As for the 2-UC MnTe (green curve in Fig. 2C), in contrast to 1-UC MnTe, it shows a uniform gap similar to Bi_2Te_3, with pronounced coherence peaks located at ±1.9 meV.

In-gap states and zero-energy modes in 1-UC MnTe/Bi_2Te_3/Fe(Te, Se)

To further investigate the spatial distributions of superconducting states, Fig. 3 (A and B) shows a surface topography and its zero-bias dI/dV map (taken at $B = 0$ T), respectively. This area contains different terraces including 1-UC MnTe, 1-UC Bi_2Te_3, and Fe(Te, Se) substrate. The zero-bias conductance (ZBC) in the 1-UC Bi_2Te_3 and Fe(Te, Se) regions are all near zero, indicating a spatially uniform superconducting gap. However, on the 1-UC MnTe surfaces, there are many separated bright regions with finite ZBC. These small regions have a typical scale of 4 to 10 nm, and we refer to them as quasiparticle "puddles" below. Panels C and D of Figure 3 show two series of dI/dV spectra taken across two puddles indicated in Fig. 3B. A clear ZECP together with multiple discrete low-energy states are seen. Their intensities decay as leaving the puddle, but the energies do not

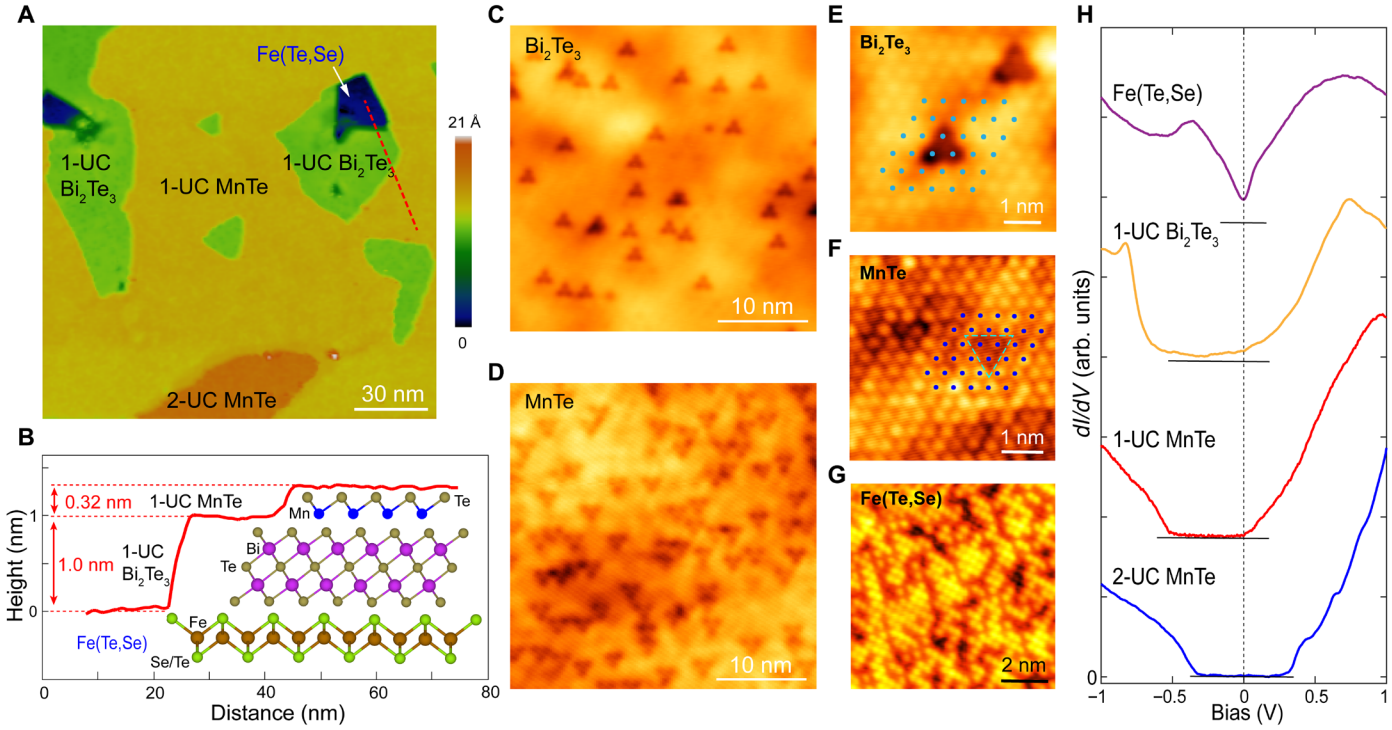

Fig. 1. The surface of MnTe/Bi_2Te_3/Fe(Te, Se) heterostructure. (**A**) Typical topographic image of the heterostructure (160 nm by 160 nm, V_b = 1 V, I = 20 pA). Different surface termination layers can be identified by different false colors. (**B**) A line profile taken along the dashed line in (A). The lattice structure of MnTe and Bi_2Te_3 layers and Fe(Te, Se) substrate are illustrated. (**C** and **D**) Topographic image of the 1-UC Bi_2Te_3 (V_b = 1 V, I = 100 pA) and 1-UC MnTe/Bi_2Te_3 surface (V_b = 1 V, I = 20 pA), respectively. (**E** to **G**) Atomically resolved images of MnTe, Bi_2Te_3, and exposed Fe(Te, Se) surface, respectively. The surface Te lattice is indicated in (E and F). (**H**) Typical large-scale dI/dV spectra taken on different surface terraces (set point: V_b = 1 V, I = 100 pA).

change obviously. Figure 3 (E to N) shows the typical spectra taken in other 10 different puddles (spots 1 to 10 in Fig. 3B). In-gap bound states and ZECPs are commonly observed. Meanwhile, the spectra taken outside puddles show a clean U-shaped gap with a size of ≈2.9 meV (spots 11 to 13; Fig. 3O). We have repeatedly observed the quasiparticle puddles with a ZECP in different 1-UC MnTe terraces (an additional dataset is shown in fig. S7). By fitting the dI/dV spectra with Gaussian peaks, we summarized the appearance probability of the in-gap states at different energies in Fig. 3P, the ZECP has a probability over 80%. The peak width [full width at half maximum (FWHM)] of the ZECP is in the range of 0.35 to 0.55 meV, which is close to the energy resolution of our system.

The quasiparticle puddles appear to distribute randomly. We have checked that the ZECP/in-gap state is not directly induced by observed defects in 1-UC MnTe (see fig. S2), and the distribution of quasiparticle puddles are also not correlated to surface defects or unevenness (see section S7 and fig. S8). This indicates that these in-gap states are unlikely the Yu-Shiba-Rusinov (YSR) state induced by impurities in MnTe. We also checked that the defects in exposed 1-UC Bi_2Te_3 do not induce YSR state either (fig. S2), which excludes that the in-gap states in 1-UC MnTe are induced by the defects of the underlying Bi_2Te_3 layer.

To explore the origin of ZECP and the in-gap states, we further measured their response to external magnetic field, elevated temperature and lowered tunneling barrier. Figure 4A shows the typical spectra measured under out-of-plane field. The ZECP persists and does not show splitting behavior up to B = 10 T (detailed analysis show that the ZECP is only slightly broadened by ~0.14 meV at B = 10 T, but substantial shift or broadening is observed for the non–zero-energy state; see section S8 and fig. S9). Meanwhile, the shape and spatial distribution of the quasiparticle puddles do not show obvious change either (fig. S10). This robustness against out-of-plane B field for ZECP also disfavors YSR-like states, which should split with a Zeeman energy (~1.1 meV for B = 10 T). Figure 4B shows a temperature dependence of the in-gap states spectra. All the in-gap states are broadened quickly at elevated temperatures and disappear near the T_C of Fe(Te, Se), which indicates that they are still quasiparticle states related to superconductivity.

It was shown that the tunneling spectra at low barrier can help clarify the nature of bound states in superconductors, e.g., a Majorana mode should have quantized conductance of $2e^2/h$ at strong coupling region and sufficiently low temperature (*45–47*). We measured the dI/dV spectra at reduced tip-sample distance via gradually increasing I_{set} at fixed V_b of 2 meV ($G_N = I_{set}/V_b$ describes the tunneling transmission). The results are summarized in Fig. 4C. As G_N increases, the ZECP maintains its position, while the side peaks gradually move to higher energy (tracked by dashed lines). The three representative spectra shown in Fig. 4 (D to F) that are taken at different G_N clearly display such behavior. Furthermore, when the conductance of ZECP reached about 0.22 ($2e^2/h$), it starts to saturate, but the side peaks keep increasing and exceed the ZECP. In Fig. 4G, we plot the ZBC as a function of G_N, and the saturation is directly evidenced. A similar behavior is also observed for other ZECPs (see fig. S11 for another dataset). We note that this behavior resembles the vortex zero modes reported in Fe(Te, Se), whose conductance are also saturated below $2e^2/h$ (*48*). It could be due to temperature

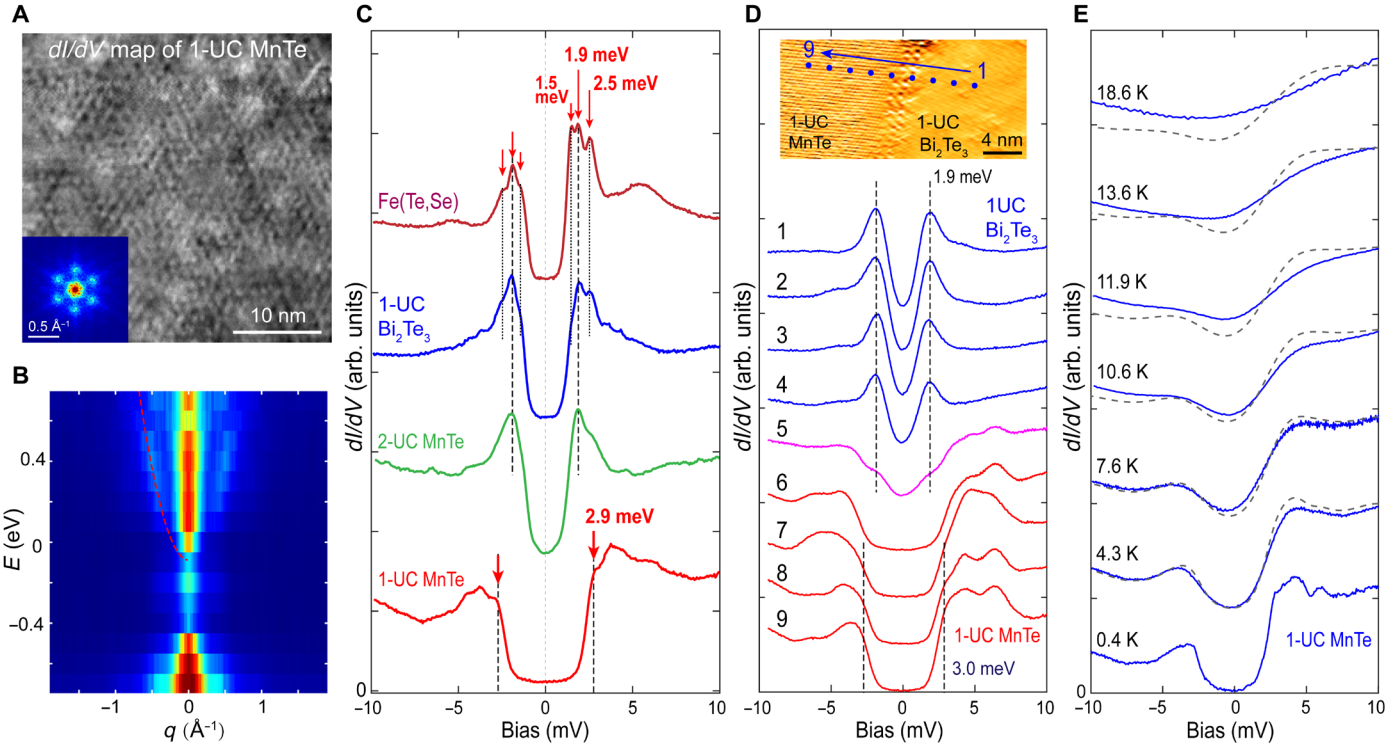

Fig. 2. The tunneling spectra and QPI of MnTe/Bi_2Te_3/Fe(Te, Se) heterostructure. (**A**) *dI/dV* map and its fast Fourier transform (FFT) image taken on 1-UC MnTe surface (V_b = 0.4 V, I = 100 pA). (**B**) Summary of the FFT line profiles taken at various energies, which shows an electron-like dispersion with a band bottom at $E_b \approx -60$ meV. (**C**) Typical superconducting gap spectra taken on different surface layers. The positions of the multiple coherence peaks are marked by arrows and tracked by dashed lines. (**D**) A series of spectra taken across a boundary between 1-UC MnTe and 1-UC Bi_2Te_3 (inset: topographic image of the boundary, the positions where the spectra were taken are marked). (**E**) Temperature dependence of the proximity superconducting gap on 1-UC MnTe. The dashed curves are convolutions of the spectrum taken at T = 0.4 K with Fermi-Dirac distribution function at corresponding temperatures.

broadening on a quantized peak, as the temperature here (T = 0.4 K) is similar to the case in (*48*).

To see detailed evolution of the in-gap states with increasing G_N, we performed Gaussian fit to the ZECP (E_0) and the two lowest side peaks (refer as $E_{\pm1}$). The fitted peak positions and peak width (FWHM) as a function of G_N are summarized in Fig. 4 (H and I, respectively). The FWHM of E_0 and $E_{\pm1}$ states all increase with G_N, and they nearly have similar values, which indicates that all these states have similar tunneling broadening at high G_N (*46*). Thus, the ZECP is distinguished from the $E_{\pm1}$ peaks for its nonshifting behavior. We notice that topologically trivial YSR states were reported to have energy shift when the tip-sample distance changes (*49*), which was attributed to tip-induced gating effect. In our heterostructure, we also occasionally observed these YSR-like shifting peaks (shown in fig. S12). Since the tunneling spectroscopy of 1-UC MnTe (Figs. 1H and 2, A and B) evidenced a bandgap and a shallow electron pocket with $k_F \approx 0.08$ (1/Å), which corresponds to a low carrier density, the tip gating could also be the cause of the shifting peaks such as $E_{\pm1}$. Therefore the nonshifting ZECP and its saturated conductance would suggest its nontrivial origin.

Absence of in-gap states and gap enhancement in 2-UC MnTe/Bi_2Te_3/Fe(Te, Se)

We also measured the superconducting state in 2-UC MnTe/Bi_2Te_3. Figure 5A shows a topographic image that contains both 1- and 2-UC MnTe terraces. The height of the second MnTe layer is similar to 1-UC MnTe (Fig. 5C). Figure 5B is the zero-bias *dI/dV* map taken on the surface of Fig. 5A. On the 1-UC MnTe region, there are similar quasiparticle puddles in which ZECPs are found (Fig. 5D, points 2 to 4). However, for the 2-UC MnTe region, no such in-gap states were observed. Its *dI/dV* spectra (Fig. 5E) display a uniform full superconducting gap with a similar shape to that of 1-UC Bi_2Te_3/Fe(Te, Se), which is also different from the enhanced gap observed in 1-UC MnTe nearby (red curve in Fig. 5E, taken on point 1 in Fig. 5B). As the large-scale spectrum of 2-UC MnTe has a wide insulating gap with E_F in the middle (Fig. 1H), the low-energy superconducting gap observed in 2-UC MnTe is likely from direct tunneling into the underneath Bi_2Te_3/Fe(Te, Se). Thus, these findings indicate that the 2-UC MnTe layer does not affect superconductivity of the system at all.

Calculations on the magnetism of 1- and 2-UC MnTe/Bi_2Te_3

The quite different superconducting states in 1- and 2-UC MnTe imply that magnetism may play an important role. Since the bulk MnTe displays interlayer AFM and intralayer ferromagnetic state (*36*, *37*), one may expect that the magnetism in 1- and 2-UC MnTe is intrinsically different. However, it is also known that magnetism could change substantially in thin film or at the interface. Therefore, we performed first-principle calculations on the magnetism of 1- and 2-UC MnTe/Bi_2Te_3 heterostructures (details are shown in section S11). First, sufficient structure optimization of 1- and 2-UC MnTe/Bi_2Te_3 were performed, and the results are shown in Fig. 6 (A to C).

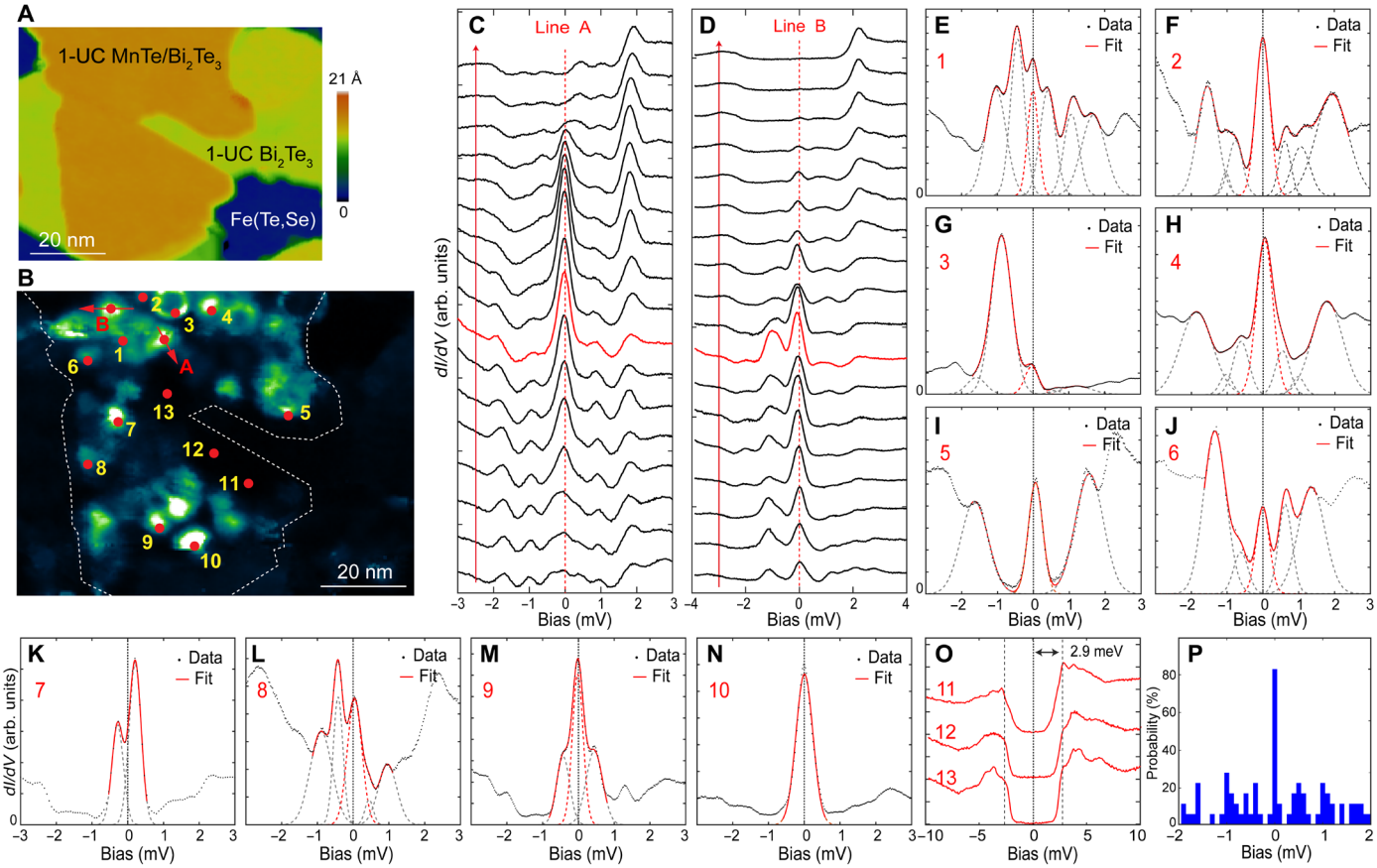

Fig. 3. ZECP and in-gap states in 1-UC MnTe/Bi_2Te_3/Fe(Te, Se). (**A**) STM image of the heterostructure (80 nm by 60 nm). (**B**) Zero-bias *dI/dV* map of the area in (A) at $B = 0$ T (set point: $V_b = 10$ mV, $I = 100$ pA). The boundary of 1-UC MnTe terrace is tracked by the white dashed curve. (**C** and **D**) *dI/dV* spectra taken along the red arrows *A* and *B* in (B), respectively (set point: $V_b = 3$ mV, $I = 200$ pA). (**E** to **O**) *dI/dV* spectra measured on numbered spots in (B). The red solid curves in each panel are Gaussian peak fitting (dashed lines are individual peaks). (**P**) Statistics of the appearance probability of the in-gap states at different energies.

They display similar in-plane lattice constant and interlayer height as that measured by STM. Then, we explore their most stable magnetic structures and evaluate the Heisenberg exchange coupling (*J*) in the local spin density approximation plus U (LSDA+U) framework. We find that 1-UC MnTe/Bi_2Te_3 favors nearest-neighbor AFM coupling (AFM1 structure) and the magnetic moment of Mn lies in plane, while the 2-UC MnTe/Bi_2Te_3 favors an interplane AFM (AFM2) with out-of-plane oriented moments, as sketched in Fig. 6 (D and E). The magnetic anisotropy energy of both the AFM1 and AFM2 states are larger than 5 meV. Since MnTe has a triangular lattice, the nearest-neighbor AFM1 state will have intrinsic frustration.

The calculated AFM1 state in 1-UC MnTe/Bi_2Te_3 is different from single UC MnTe in the bulk form. This is checked to be due to interfacial effect (e.g. lattice strain), as our calculation can correctly predict the in-plane AFM state of bulk MnTe (see the Supplementary Materials). However, the above LSDA+U calculations only involve Heisenberg interactions, while for magnetic systems without inversion symmetry (such as heterostructures), SOC should give rise to DMIs that favor twisted spin configuration. On the basis of a first-principles linear response (FPLR) approach, we further calculated the DMI together with Heisenberg parameters of 1-UC MnTe/Bi_2Te_3 (section S11). The Heisenberg coupling (*J*) estimated by FPLR agrees well with that calculated by LSDA+U (≈20.0 meV). Meanwhile, the strength of nearest-neighbor DMI $|D|$ is estimated to be 4.2 meV (specific values of the **D** vector are shown in table S6). Such a large DMI is originated from the large SOC of Bi_2Te_3 and the inversion asymmetric interface. We notice that several recent theoretical works on the structural asymmetric Mn dichalcogenide also give very large DMI (*31*, *32*).

DISCUSSION

The robust ZECPs with nontrivial properties and enhanced superconducting gap in 1-UC MnTe/Bi_2Te_3/Fe(Te, Se) are rather unconventional phenomena. Below, we will discuss their origin. First, the observed ZECPs are located inside of the MnTe terrace, not at the edge. This excludes their origin of chiral edge mode that was predicted for ferromagnet/TI/superconductor heterostructures (*24*, *25*). A natural explanation is that the 1-UC MnTe here is not ferromagnetic, as shown by above calculations. Second, these randomly distributed ZECPs seem to resemble the tunneling spectra of previously reported ferromagnet/superconductor heterostructures (*5*, *6*), in which ZECPs were also observed and were attributed to spin-triplet pairing state (*1*, *2*). However, we notice that this spin-triplet state would require a spin rotation at the interface (i.e., misalignment between the interfacial spin and bulk magnetization of the ferromagnet layer) and

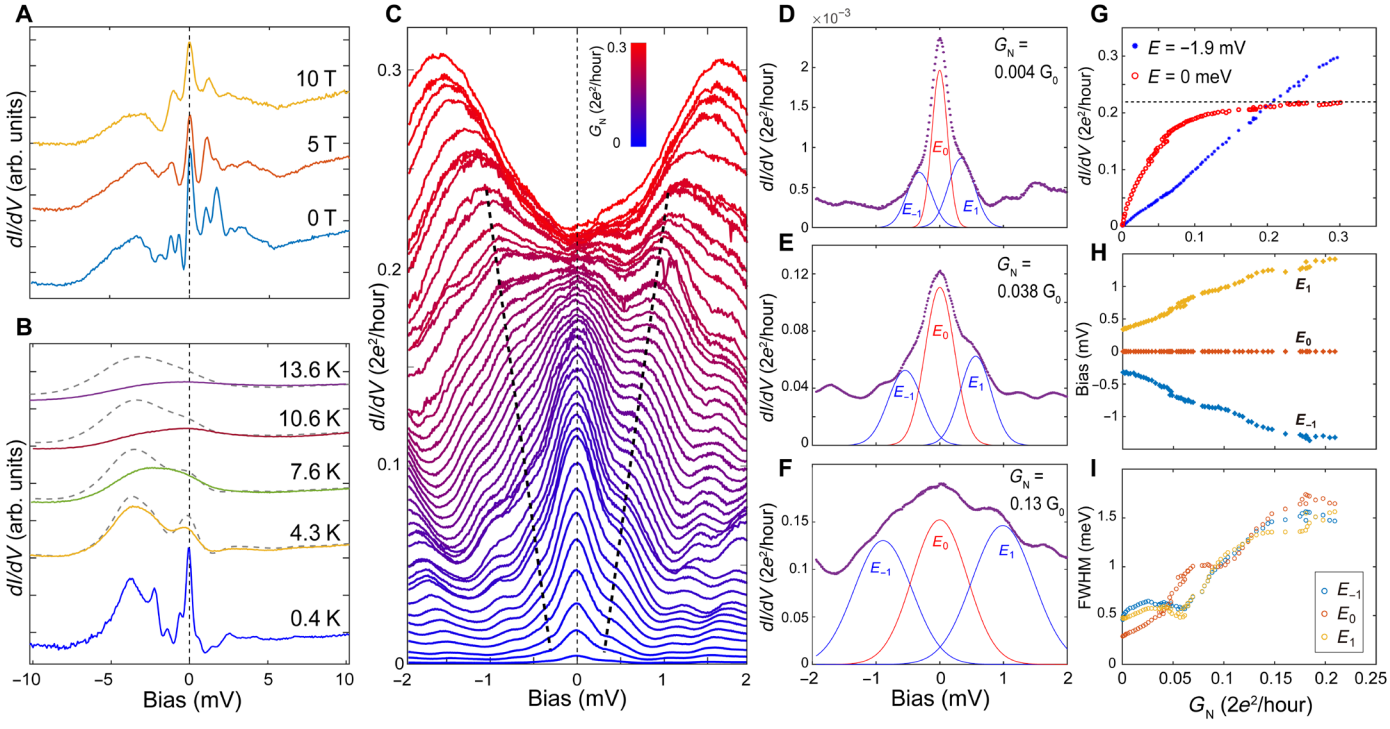

Fig. 4. Magnetic field, temperature, and tunneling transmission dependence of the in-gap states and ZECP. (**A**) *dI/dV* spectra taken at the same quasiparticle puddle in 1-UC MnTe under different magnetic field (V_b = 10 mV, I = 200 pA). (**B**) Temperature dependence of the *dI/dV* spectra with in-gap states (dashed curves are convolutions of the T = 0.4 K spectrum with the Fermi-Dirac distribution at elevated temperatures). (**C**) Evolution of *dI/dV* spectra with increasing tunneling transmission G_N ($G_N = I_{set}/V_b$, V_b = 2 mV). (**D** to **F**) Representative *dI/dV* spectra taken at different G_N, and the Gaussian fit to the three low-energy peaks (referred by $E_{\pm1}$, E_0). (**G**) The tunneling conductance at 0 and −1.9 mV as a function of G_N. The absolute conductance value is calibrated by numerical differential of the *I/V* curve. (**H** and **I**) Energy positions and peak width (FWHM) of three fitted peaks (E_0, $E_{\pm1}$) as a function of G_N, respectively.

therefore is usually sensitive to external magnetic field (*5*, *6*). In our measurement, the ZECP is robust against magnetic field (at least for out-of-plane field), and the MnTe layer is only 1 UC thick, which is unlikely to give interfacial spin misalignment. Thus, the spin-triplet pairing scenario is also not favored here.

Then, the above calculations of magnetism can provide an alternative explanation. It was shown that DMI and frustrated AFM state can both promote (in-plane) noncolinear spin texture such as skyrmions (*50*–*52*). Here, the calculated DMI strength in 1-UC MnTe/Bi_2Te_3 is even larger than that of the Co/Pt (≈3.0 meV) and Fe/Ir (≈1.7 meV) thin films (*53*, *54*), in which skyrmions were observed with a typical size down to a few nanometers. Recently, a number of theoretical works have shown that various types of noncolinear spin texture can induce unconventional pairings in magnet/superconducting interface, which often manifest themselves as in-gap states (*10*–*19*). Particularly, zero-energy modes can be induced inside of ferromagnetic skyrmions (*11*, *12*, *14*) or at the end of AFM skyrmion chains under certain conditions (*17*). Here, the ZECPs/in-gap states in 1-UC MnTe/Bi_2Te_3/Fe(Te, Se) are distributed in separated regions with a typical size of 4 to 10 nm (Fig. 3 and fig. S7). As defect-induced YSR states are not the origin, they are likely induced by certain noncolinear spin textures residing in such length scale. Moreover, the in-plane oriented magnetic moments in AFM1 state with strong anisotropy energy (>5 meV) suggest that they should be robust against out-of-plane field, which is consistent with our measurement in Fig. 4A. For 2-UC MnTe/Bi_2Te_3/Fe(Te, Se), the interplane AFM2 state with out-of-plane oriented moments is not frustrated and its interfacial DMI will also be weaker. Therefore, one expects to see less affected superconductivity in 2-UC MnTe.

Besides, the enhanced superconducting gap in 1-UC MnTe is another remarkable founding. To our knowledge, this is a very rare case that a proximity induced gap in magnetic material can be notably larger than the host superconductor. Most tunneling measurements on magnet/superconductor heterostructures have reported a reduced gap (*5*, *26*–*28*). Here, since a shallow electron pocket crossed E_F in 1-UC MnTe (Fig. 2B), it indicates that the conducting electrons in 1-UC MnTe participated in superconductivity. Thus, our results indicate that interfacial 1-UC MnTe layer is a "doped AFM insulator." We notice that the electron correlation in MnTe (in which the Mn atoms have $3d^5$ configuration) was reported to be strong (*55*). The gap enhancement mechanism could be related to the frustrated magnetism and electron correlations in 1-UC MnTe, which is quite interesting and worthy of further investigation. As for the 2-UC MnTe, since its E_F is well inside the insulating gap and the magnetism is also different, the gap enhancement is absent.

Last, we shall point out another possibility for observing in-gap states at B = 0 T: the "spontaneous" vortex state that was suggested for certain ferromagnet/superconductor interface (*56*) or superconductors with magnetic impurities (*44*, *57*, *58*). If assuming 1-UC MnTe only provides an effective magnetic field to the underneath Bi_2Te_3/Fe(Te, Se) and generated the in-gap state/ZECP, then one would expect to see similar ZECP in vortex of 1-UC Bi_2Te_3 by applying an external field. We have checked the vortex states of 1-UC Bi_2Te_3/Fe(Te, Se) (fig. S6), which show that there is a broad peak

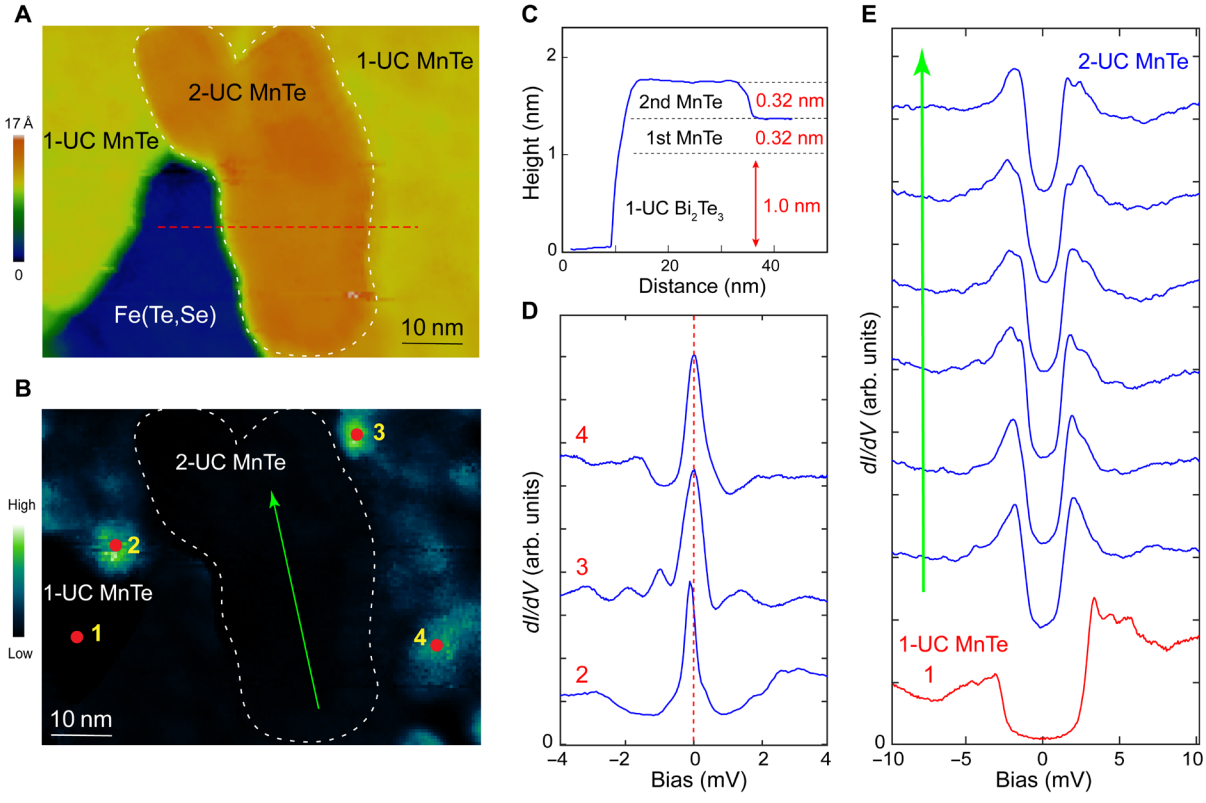

Fig. 5. STM characterization of 2-UC MnTe/Bi_2Te_3/Fe(Te, Se). (**A**) Topological image including a 2-UC MnTe terrace (53 nm by 70 nm, $V_b = 1$ V, $I = 20$ pA). The white dashed curve indicates the edge of 2-UC MnTe terrace. (**B**) Zero-bias *dI/dV* map taken in the area of (A) (set point: $V_b = 10$ mV, $I = 150$ pA). (**C**) The height profile along the red dashed line in (A). (**D**) *dI/dV* spectra measured at the 1-UC MnTe regions that show a ZECP [on the spots 2 to 4 in (B)]. (**E**) A series of *dI/dV* taken along the green arrow in (B) (on 2-UC MnTe), and the spectrum taken on spot 1 in (B) (on 1-UC MnTe; set point: $V_b = 10$ mV, $I = 150$ pA)

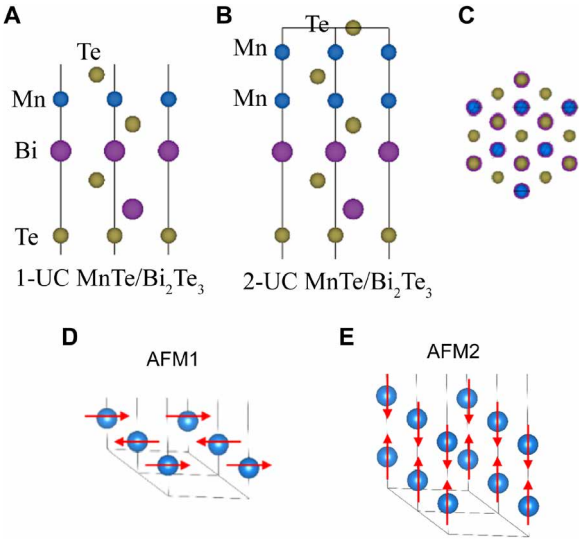

Fig. 6. Calculated magnetic structure of 1- and 2-UC MnTe on Bi_2Te_3. (**A** and **B**) Side views of optimized structure of 1- and 2-UC MnTe/Bi_2Te_3 interface, respectively. The blue, purple, and yellow balls represent Mn, Bi, and Te atoms, respectively. (**C**) Top view of the interface. (**D** and **E**) Local magnetic structure of 1-UC MnTe/Bi_2Te_3 and 2-UC MnTe/Bi_2Te_3, respectively.

near zero bias at vortex center, and it gradually splits as leaving the vortex. This behavior is similar to that previously observed in Bi_2Te_3/Fe(Te, Se) (*39*, *40*) and Bi_2Te_3/$NbSe_2$ systems (*59*) but very different from the multiple in-gap states and nonsplitting ZECP in 1-UC MnTe here. Therefore, the spontaneous vortex state scenario is also not favored.

In summary, we have successfully fabricated a trilayer-type magnet-superconductor heterostructure of MnTe/Bi_2Te_3/Fe(Te, Se) that has atomically sharp interface and in which strong SOC is intentionally introduced. The observation of robust zero-energy modes and enhanced superconducting gap in 1-UC MnTe region strongly suggest an unconventional pairing state. Via first-principle calculations, we show that 1-UC MnTe/Bi_2Te_3 has large DMI due to its inversion asymmetric structure and strong SOC, which can generate noncolinear spin textures and give rise to ZECP. The enhanced gap could also be related to the frustrated magnetism and electron correlations in 1-UC MnTe. Therefore, this heterostructure provides a promising platform for further exploring unconventional and topological nontrivial superconductivity.

MATERIALS AND METHODS

Growth of the heterostructure

The sample growth was conducted in a low-temperature STM system (UNISOKU 1300) equipped with an MBE chamber. The $FeTe_xSe_{1-x}$ ($x \approx 0.55$) single crystal with $T_C = 14.5$ K was cleaved in a UHV

chamber at 78 K. Bi_2Te_3 (1 UC) was first grown on cleaved surface by co-depositing Bi (99.997%) and Te (99.999%) with a flux ratio of ≈1:10. Then, 1- to 2-UC MnTe was grown by co-depositing Mn (99.95%) and Te (99.999%) with a flux ratio of ≈1:10. The substrate was kept at 200°C during the growth and was post-annealed at the same temperature for 10 min to further improve the quality. The sample was transferred in situ from the MBE chamber to STM chamber after growth.

STM measurement

STM experiments were conducted at $T = 0.4$ or 4.2 K. PrIr tip was used after treatment on the Au(111) surface. The dI/dV spectra were collected by a standard lock-in technique with a modulation frequency of 741 Hz and amplitudes (ΔV) of 0.5 mV at 4.2 K and 0.1 mV at 0.4 K. The energy resolution and the zero point of sample bias were calibrated before measurement (fig. S1).

SUPPLEMENTARY MATERIALS

Supplementary material for this article is available at https://science.org/doi/10.1126/sciadv.abq4578

REFERENCES AND NOTES

1. A. I. Buzdin, Proximity effects in superconductor-ferromagnet heterostructures. *Rev. Mod. Phys.* **77**, 935–976 (2005).
2. F. S. Bergeret, A. F. Volkov, K. B. Efetov, Odd triplet superconductivity and related phenomena in superconductor-ferromagnet structures. *Rev. Mod. Phys.* **77**, 1321–1373 (2005).
3. J. Linder, J. W. A. Robinson, Superconducting spintronics. *Nat. Phys.* **11**, 307–315 (2015).
4. M. Eschrig, Spin-polarized supercurrents for spintronics: A review of current progress. *Rep. Prog. Phys.* **78**, 104501 (2015).
5. A. Bernardo, S. Diesch, Y. Gu, J. Linder, G. Divitini, C. Ducati, E. Scheer, M. G. Blamire, J. W. A. Robinson, Signature of magnetic-dependent gapless odd frequency states at superconductor/ferromagnet interfaces. *Nat. Commun.* **6**, 8053 (2015).
6. S. Diesch, P. Machon, M. Wolz, C. Sürgers, D. Beckmann, W. Belzig, E. Scheer, Creation of equal-spin triplet superconductivity at the Al/EuS interface. *Nat. Commun.* **9**, 5248 (2018).
7. S. Nadj-Perge, I. K. Drozdov, J. Li, H. Chen, S. Jeon, J. Seo, A. H. MacDonald, B. A. Bernevig, A. Yazdani, Observation of Majorana fermions in ferromagnetic atomic chains on a superconductor. *Science* **346**, 602–607 (2014).
8. K. Pöyhönen, A. Weststrom, J. Röntynen, T. Ojanen, Majorana states in helical Shiba chains and ladders. *Phys. Rev. B* **89**, 115109 (2014).
9. J. Li, T. Neupert, Z. Wang, A. H. MacDonald, A. Yazdani, B. A. Bernevig, Two-dimensional chiral topological superconductivity in Shiba lattices. *Nat. Commun.* **7**, 12297 (2016).
10. S. Nakosai, Y. Tanaka, N. Nagaosa, Two-dimensional p-wave superconducting states with magnetic moments on a conventionals-wave superconductor. *Phys. Rev. B* **88**, 180503 (2013).
11. W. Chen, A. P. Schnyder, Majorana edge states in superconductor-noncollinear magnet interfaces. *Phys. Rev. B* **92**, 214502 (2015).
12. G. Yang, P. Stano, J. Klinovaja, D. Loss, Majorana bound states in magnetic skyrmions. *Phys. Rev. B* **93**, 224505 (2016).
13. S. S. Pershoguba, S. Nakosai, A. V. Balatsky, Skyrmion-induced bound states in a superconductor. *Phys. Rev. B* **94**, 064513 (2016).
14. M. Garnier, A. Mesaros, P. Simon, Topological superconductivity with deformable magnetic skyrmions. *Commun. Phys.* **2**, 126 (2019).
15. K. M. D. Hals, M. Schecter, M. S. Rudner, Composite topological excitations in ferromagnet-superconductor heterostructures. *Phys. Rev. Lett.* **117**, 017001 (2016).
16. T. Zhou, N. Mohanta, J. E. Han, A. Matos-Abiague, I. Žutić, Tunable magnetic textures in spin valves: From spintronics to Majorana bound states. *Phys. Rev. B* **99**, 134505 (2019).
17. S. A. Diaz, J. Klinovaja, D. Loss, S. Hoffman, Majorana bound states induced by antiferromagnetic Skyrmion textures. arXiv:2102.03423 [cond-mat.str-el] (5 February 2021).
18. E. Mascot, J. Bedow, M. Graham, S. Rachel, D. K. Morr, Topological superconductivity in skyrmion lattices. *npj Quant. Mater.* **6**, 6 (2021).
19. A. O. Zlotnikov, M. S. Shustin, A. D. Fedoseev, Aspects of topological superconductivity in 2D systems: noncollinear magnetism, skyrmions, and higher-order topology. arXiv:2109.03169 [cond-mat.supr-con] (7 September 2021).
20. V. Mourik, K. Zuo, S. M. Frolov, S. R. Plissard, E. P. A. M. Bakkers, L. P. Kouwenhoven, Signatures of Majorana fermions in hybrid superconductor semiconductor nanowire devices. *Science* **336**, 1003–1007 (2012).
21. A. Das, Y. Ronen, Y. Most, Y. Oreg, M. Heiblum, H. Shtrikman, Zero-bias peaks and splitting in an Al–InAs nanowire topological superconductor as a signature of Majorana fermions. *Nat. Phys.* **8**, 887–895 (2012).
22. N. Nagaosa, Y. Tokura, Topological properties and dynamics of magnetic skyrmions. *Nat. Nanotechnol.* **8**, 899–911 (2013).
23. A. Fert, N. Reyren, V. Cros, Magnetic skyrmions: Advances in physics and potential applications. *Nat. Rev. Mater.* **2**, 17031 (2017).
24. J. J. He, T. Liang, Y. Tanaka, N. Nagaosa, Platform of chiral Majorana edge modes and its quantum transport phenomena. *Commun. Phys.* **2**, 149 (2019).
25. X. Zhang, F. Liu, Prediction of Majorana edge states from magnetized topological surface states. *Phys. Rev. B* **103**, 024405 (2021).
26. G. C. Ménard, S. Guissart, C. Brun, R. T. Leriche, M. Trif, F. Debontridder, D. Demaille, D. Roditchev, P. Simon, T. Cren, Two-dimensional topological superconductivity in Pb/Co/Si(111). *Nat. Commun.* **8**, 2040 (2017).
27. A. Palacio-Morales, E. Mascot, S. Cocklin, H. Kim, S. Rachel, D. K. Morr, R. Wiesendanger, Atomic-scale interface engineering of Majorana edge modes in a 2D magnet-superconductor hybrid system. *Sci. Adv.* **5**, eaav6600 (2019).
28. S. Kezilebieke, M. N. Huda, P. Dreher, I. Manninen, Y. Zhou, J. Sainio, R. Mansell, M. M. Ugeda, S. van Dijken, H. P. Komsa, P. Liljeroth, Electronic and magnetic characterization of epitaxial VSe_2 monolayers on superconducting $NbSe_2$. *Commun. Phys.* **3**, 116 (2020).
29. S. Kezilebieke, M. N. Huda, V. Vaño, M. Aapro, S. C. Ganguli, O. J. Silveira, S. Głodzik, A. S. Foster, T. Ojanen, P. Liljeroth, Topological superconductivity in a van der Waals heterostructure. *Nature* **588**, 424–428 (2020).
30. A. Fert, V. Cros, J. Sampaio, Skyrmions on the track. *Nat. Nanotechnol.* **8**, 152–156 (2013).
31. J. Yuan, Y. Yang, Y. Cai, Y. Wu, Y. Chen, X. Yan, L. Shen, Intrinsic skyrmions in monolayer Janus magnets. *Phys. Rev. B* **101**, 094420 (2020).
32. J. Liang, W. Wang, H. du, A. Hallal, K. Garcia, M. Chshiev, A. Fert, H. Yang, Very large Dzyaloshinskii-Moriya interaction in two-dimensional Janus manganese dichalcogenides and its application to realize skyrmion states. *Phys. Rev. B* **101**, 184401 (2020).
33. J. Chen, L. Wang, M. Zhang, L. Zhou, R. Zhang, L. Jin, X. Wang, H. Qin, Y. Qiu, J. Mei, F. Ye, B. Xi, H. He, B. Li, G. Wang, Evidence for magnetic skyrmions at the interface of ferromagnet/topological-insulator heterostructures. *Nano Lett.* **19**, 6144–6151 (2019).
34. Q. L. He, G. Yin, A. J. Grutter, L. Pan, X. Che, G. Yu, D. A. Gilbert, S. M. Disseler, Y. Liu, P. Shafer, B. Zhang, Y. Wu, B. J. Kirby, E. Arenholz, R. K. Lake, X. Han, K. L. Wang, Exchange-biasing topological charges by antiferromagnetism. *Nat. Commun.* **9**, 2767 (2018).
35. H. Wu, F. Groß, B. Dai, D. Lujan, S. A. Razavi, P. Zhang, Y. Liu, K. Sobotkiewich, J. Förster, M. Weigand, G. Schütz, X. Li, J. Gräfe, K. L. Wang, Ferrimagnetic skyrmions in topological insulator/ferrimagnet heterostructures. *Adv. Mater.* **32**, 2003380 (2020).
36. D. Kriegner, K. Výborný, K. Olejník, H. Reichlová, V. Novák, X. Marti, J. Gazquez, V. Saidl, P. Němec, V. V. Volobuev, G. Springholz, V. Holý, T. Jungwirth, Multiple-stable anisotropic magnetoresistance memory in antiferromagnetic MnTe. *Nat. Commun.* **7**, 11623 (2016).
37. D. Kriegner, H. Reichlova, J. Grenzer, W. Schmidt, E. Ressouche, J. Godinho, T. Wagner, S. Y. Martin, A. B. Shick, V. V. Volobuev, G. Springholz, V. Holý, J. Wunderlich, T. Jungwirth, K. Výborný, Magnetic anisotropy in antiferromagnetic hexagonal MnTe. *Phys. Rev. B* **96**, 214418 (2017).
38. H. J. Zhang, C.-X. Liu, X.-L. Qi, X. Dai, Z. Fang, S.-C. Zhang, Topological insulators in Bi_2Se_3, Bi_2Te_3 and Sb_2Te_3 with a single Dirac cone on the surface. *Nat. Phys.* **5**, 438–442 (2009).
39. H. Zhao, B. Rachmilowitz, Z. Ren, R. Han, J. Schneeloch, R. Zhong, G. Gu, Z. Wang, I. Zeljkovic, Superconducting proximity effect in a topological insulator using Fe(Te, Se). *Phys. Rev. B* **97**, 224504 (2018).
40. M. Chen, X. Chen, H. Yang, Z. Du, H.-H. Wen, Superconductivity with twofold symmetry in $Bi_2Te_3/FeTe_{0.55}Se_{0.45}$ heterostructure. *Sci. Adv.* **4**, eaat1084 (2018).
41. Y. Gong, J. Guo, J. Li, K. Zhu, M. Liao, X. Liu, Q. Zhang, L. Gu, L. Tang, X. Feng, D. Zhang, W. Li, C. Song, L. Wang, P. Yu, X. Chen, Y. Wang, H. Yao, W. Duan, Y. Xu, S. C. Zhang, X. Ma, Q. K. Xue, K. He, Experimental realization of an intrinsic magnetic topological insulator. *Chin. Phys. Lett.* **36**, 076801 (2019).
42. A. V. Matetskiy, I. A. Kibirev, T. Hirahara, S. Hasegawa, A. V. Zotov, A. A. Saranin, Direct observation of a gap opening in topological interface states of $MnSe/Bi_2Se_3$ heterostruture. *Appl. Phys. Lett.* **107**, 091604 (2015).
43. J. Teng, N. Liu, Y. Li, Mn-doped topological insulators: A review. *J. Semicond.* **40**, 081507 (2019).
44. J. X. Yin, Z. Wu, J.-H. Wang, Z.-Y. Ye, J. Gong, X.-Y. Hou, L. Shan, A. Li, X.-J. Liang, X.-X. Wu, J. Li, C.-S. Ting, Z.-Q. Wang, J.-P. Hu, P.-H. Hor, H. Ding, S. H. Pan, Observation of a robust zero-energy bound state in iron-based superconductor Fe(Te, Se). *Nat. Phys.* **11**, 543–546 (2015).
45. K. T. Law, P. A. Lee, T. K. Ng, Majorana fermion induced resonant Andreev reflection. *Phys. Rev. Lett.* **103**, 237001 (2009).
46. F. Setiawan, C. X. Liu, J. D. Sau, S. das Sarma, Electron temperature and tunnel coupling dependence of zero-bias and almost-zero-bias conductance peaks in Majorana nanowires. *Phys. Rev. B* **96**, 184520 (2017).

47. C. Chen, Q. Liu, T. Z. Zhang, D. Li, P. P. Shen, X. L. Dong, Z.-X. Zhao, T. Zhang, D. L. Feng, Quantized conductance of Majorana zero mode in the vortex of the topological superconductor ($Li_{0.84}Fe_{0.16}$)OHFeSe. *Chin. Phys. Lett.* **36**, 057403 (2019).
48. S. Y. Zhu, L. Kong, L. Cao, H. Chen, M. Papaj, S. Du, Y. Xing, W. Liu, D. Wang, C. Shen, F. Yang, J. Schneeloch, R. Zhong, G. Gu, L. Fu, Y.-Y. Zhang, H. Ding, H.-J. Gao, Nearly quantized conductance plateau of vortex zero mode in an iron-based superconductor. *Science* **367**, 189 (2020).
49. D. Chatzopoulos, D. Cho, K. M. Bastiaans, G. O. Steffensen, D. Bouwmeester, A. Akbari, G. Gu, J. Paaske, B. M. Andersen, M. P. Allan, Spatially dispersing Yu-Shiba-Rusinov states in the unconventional superconductor $FeTe_{0.55}Se_{0.45}$. *Nat. Commun.* **12**, 298 (2021).
50. H. D. Rosales, D. C. Cabra, P. Pujol, Three-sublattice skyrmion crystal in the antiferromagnetic triangular lattice. *Phys. Rev. B* **92**, 214439 (2015).
51. M. Mohylna, J. Buša Jr., M. Žukovič, Formation and growth of skyrmion crystal phase in a frustrated Heisenberg antiferromagnet with Dzyaloshinskii-Moriya interaction. *J. Magn. Magn. Mater.* **527**, 167755 (2021).
52. Z. Liu, M. dos Santos Dias, S. Lounis, Theoretical investigation of antiferromagnetic skyrmions in a triangular monolayer. *J. Phys.: Condens. Matter* **32**, 425801 (2020).
53. O. Boulle, J. Vogel, H. Yang, S. Pizzini, D. de Souza Chaves, A. Locatelli, T. O. Menteş, A. Sala, L. D. Buda-Prejbeanu, O. Klein, M. Belmeguenai, Y. Roussigné, A. Stashkevich, S. M. Chérif, L. Aballe, M. Foerster, M. Chshiev, S. Auffret, I. M. Miron, G. Gaudin, Room-temperature chiral magnetic skyrmions in ultrathin magnetic nanostructures. *Nat. Nanotechnol.* **11**, 449–454 (2016).
54. B. Dupé, M. Hoffmann, C. Paillard, S. Heinze, Tailoring magnetic skyrmions in ultra-thin transition-metal films. *Nat. Commun.* **5**, 4030 (2014).
55. S. J. Youn, B. I. Min, A. J. Freeman, Crossroads electronic structure of MnS, MnSe, and MnTe. *Phys. Stat. Sol. (b)* **241**, 1411–1414 (2004).
56. M. Iavarone, A. Scarfato, F. Bobba, M. Longobardi, G. Karapetrov, V. Novosad, V. Yefremenko, F. Giubileo, A. M. Cucolo, Imaging the spontaneous formation of vortex-antivortex pairs in planar superconductor/ferromagnet hybrid structures. *Phys. Rev. B* **84**, 024506 (2011).
57. K. Jiang, X. Dai, Z. Wang, Quantum anomalous vortex and majorana zero mode in iron-based superconductor Fe(Te, Se). *Phys. Rev. X* **9**, 011033 (2019).
58. P. Fan, F. Yang, G. Qian, H. Chen, Y.-Y. Zhang, G. Li, Z. Huang, Y. Xing, L. Kong, W. Liu, K. Jiang, C. Shen, S. du, J. Schneeloch, R. Zhong, G. Gu, Z. Wang, H. Ding, H.-J. Gao, Observation of magnetic adatom-induced Majorana vortex and its hybridization with field-induced Majorana vortex in an iron-based superconductor. *Nat. Commun.* **12**, 1348 (2021).
59. J.-P. Xu, M.-X. Wang, Z.-L. Liu, J.-F. Ge, X. Yang, C. Liu, Z. A. Xu, D. Guan, C. L. Gao, D. Qian, Y. Liu, Q.-H. Wang, F.-C. Zhang, Q.-K. Xue, J.-F. Jia, Experimental detection of a majorana mode in the core of a magnetic vortex inside a topological insulator-superconductor $Bi_2Te_3/NbSe_2$ heterostructure. *Phys. Rev. Lett.* **114**, 017001 (2015).

Acknowledgments: We thank X. Dai and T. K. NG for helpful discussions. **Funding:** This work is supported by the National Key R&D Program of the MOST of China (grant nos. 2017YFA0303004 and 2018YFA0704300), the Innovation Program for Quantum Science and Technology (grant no. 2021ZD0302800), the National Natural Science Foundation of China (grant nos. 92065202, 11888101, 11790312, 11961160717, and U1932217), the Science Challenge Project (grant no. TZ2016004), the Shanghai Municipal Science and Technology Major Project (grant no. 2019SHZDZX01), the Shanghai Pilot Program for Basic Research, Fudan University 21TQ1400100 (21TQ005), and the China Postdoctoral Science Foundation (grant no. BX20200097). **Author contributions:** The growth of heterostructure and STM measurement: S.D., C.C., R.T., D.Z., Y.H., T.J., and Y.Y. Fe(Te, Se) single crystal growth: Y.P. and Z.S. First-principle calculation: Z.C., D.W., and X.W. Supervision: D.F. and T.Z. Writing: D.F., X.W., and T.Z. All authors have discussed the results and the interpretation. **Competing interests:** The authors declare that they have no competing interests. **Data and materials availability:** All data needed to evaluate the conclusions in the paper are present in the paper and/or the Supplementary Materials.

Submitted 16 April 2022
Accepted 28 July 2022
Published 14 September 2022
10.1126/sciadv.abq4578